



In-situ growth of graphene decorations for high-performance LiFePO₄ cathode through solid-state reaction



Jing Li, Li Zhang*, Longfei Zhang, Weiwei Hao, Haibo Wang, Qunting Qu, Honghe Zheng*

School of Energy, Soochow University, Suzhou, Jiangsu 215006, PR China

HIGHLIGHTS

- Graphene-decorated LiFePO₄ is *in-situ* synthesized through solid-state reaction.
- Graphene is *in-situ* grown through pyrolysis and catalytic graphitization of glucose.
- Graphene forms a compact, uniform and thin coating layer throughout the LFP NPs.
- Graphene cross-links into a conducting network around the LFP NPs.
- Electrochemical performance of LFP@graphene is remarkably improved.

GRAPHICAL ABSTRACT



ARTICLE INFO

Article history:

Received 11 September 2013

Received in revised form

5 October 2013

Accepted 24 October 2013

Available online 5 November 2013

Keywords:

Graphene

In-situ growth

Li-ion batteries

Lithium iron phosphate cathode

Solid-state reaction

ABSTRACT

Graphene-decorated LiFePO₄ composite is synthesized for the first time through *in-situ* pyrolysis and catalytic graphitization, in which glucose and a trace amount of FeSO₄ are employed as the graphene source and catalyst precursor, respectively. Under Ar/H₂ (95:5) atmosphere at 750 °C, FeSO₄ is thermally reduced to Fe nano-particles (Fe NPs) and glucose is pyrolyzed to carbon fragments first, followed by the *in-situ* growth of graphene sheets directly on the LiFePO₄ nano-particles (LFP NPs) surface through the realignment of carbon fragments under the catalytic effect of the Fe NPs. The graphene sheets not only form a compact and uniform coating layer throughout the LFP NPs, but also stretch out and cross-link into a conducting network around the LFP particles. The LiFePO₄@graphene composite displays a high reversible specific capacity of 167.7 mAh g⁻¹ at 0.1C rate, superb rate performance with discharge capacity of 94.3 mAh g⁻¹ at 100C rate and much prolonged cycle life. The remarkable electrochemical improvement is attributed to both electric and ionic conductivity increase as a result of *in-situ* grown graphene coatings along the LFP surface and the graphene network intrinsically connecting to the LFP particles.

© 2013 Elsevier B.V. All rights reserved.

1. Introduction

The olivine-structured LiFePO₄ (LFP) is widely accepted as a promising cathode candidate used in lithium-ion batteries (LIBs) for powering electric vehicles (EVs) and plug-in hybrid electric

vehicles (PHEVs) due to its high theoretical capacity (170 mAh g⁻¹), acceptable operating voltage (3.4 V vs. Li⁺/Li), good safety, low cost and toxicity [1–9]. However, one of the major challenges for the commercialization of LFP is the poor high-rate capability, attributed to its intrinsically low electronic conductivity (10⁻⁹–10⁻¹⁰ S cm⁻¹) and slow ionic diffusivity (~10⁻¹⁴ cm² s⁻¹) [10–12]. Considerable efforts have been made to overcome the electronic and ionic transport limitations of LFP by reducing the particle size, [13–15] optimizing the morphology [16,17], decorating the surface with

* Corresponding authors. Tel.: +86 512 69153523.

E-mail addresses: zhangli81@suda.edu.cn (L. Zhang), hzhzheng@suda.edu.cn (H. Zheng).

electrically conducting agents [11,18–22] and doping the host framework with supervalent cations [23–25]. Among these strategies, a combination of nano-sized particles and carbon coating is considered as the most effective route to improve the material utilization and rate performance of LFP cathode [26–28]. Particle size reduction provides both a shorter diffusion path and a large surface area for charge carriers, resulting in a higher ionic diffusion constant. Furthermore, carbon coating not only enhances the surface electrical conductivity and thus alleviating the electrode polarization, but also prevents the iron dissolution and migration [29]. All these factors contribute to great improvements of the reversible capacity, cycling stability and rate capability [26,27].

Although carbon coating of LFP has been extensively studied and successfully commercialized, there still remain several fundamental and technical questions. It is well known that various parameters of carbon coating layer including carbon content, degree of graphitization and morphology, coating thickness, distribution (uniformity and coverage) and carbon surface area can significantly affect the electrochemical performance of LFP cathode [26,27,30–33]. Typically, a thin, uniform and highly-graphitic carbon coating layer throughout the LFP nano-particles (LFP NPs) is regarded as the most promising coating manner for LFP cathode with high electrochemical performance [26,27,34–36]. In addition, intrinsic interconnection between carbon coating layers is also very effective to reduce the contact resistance between active material particles. On the other hand, the graphitic carbon coating layer needs to be very thin (1–3 nm) to allow easy and rapid penetration of Li^+ ions [26,27]. Nevertheless, developing an effective approach to produce ultrathin and uniform graphitic carbon coatings is very challenging given carbon is difficult to graphitize at relatively low temperatures required for synthesis of LFP (600–800 °C) [26,34–36].

Recent studies have introduced graphene as a two-dimensional (2D) graphitic carbon nano-material in the LFP cathode in order to produce a three-dimensional (3D) conducting matrix [37–47]. However, the specific capacity and rate performance of LFP/graphene composite were not significantly improved compared to the amorphous carbon coated LFP [42,47]. The main reason is that LFP particles just loosely contact with the graphene frames. When the LFP particles were tightly anchored onto and entirely encapsulated into highly graphitized graphene sheets, the electrical conductivity of LFP can be greatly enhanced at the expense of hindering the quick transport of the Li^+ ions to the active materials. Several groups have proposed a coating strategy solution by combining a complete carbon coating layer and a cross-linked graphene conducting network outside the LFP particles. The graphene network plays a key role in providing good inter-particle electrical connection and creating available voids for electrolyte storage and Li^+ ions transport [37–39]. In terms of the graphene-based composite materials, chemically exfoliated graphene oxide (GO) or reduced graphene oxide (RGO) sheets are so far the preferred choice [26,37–47]. This choice leads to two major technical problems: first, GO and RGO need to be specially produced prior to the synthesis of the final product; second, achieving uniform dispersion (or growth) of LFP or carbon coated LFP within the crumpled micrometer-size graphene sheets is difficult or almost impossible with graphene sheets and LFP produced separately.

To overcome the shortcomings in the composite architecture and preparation technology of the carbon-coated LFP, we designed a bottom-up strategy to synthesize a graphene-decorated LiFePO_4 composite (LFP@graphene) through an *in-situ* pyrolysis and catalytic graphitization process. Glucose and a trace amount of FeSO_4 were employed as the graphene source and catalyst precursors, respectively. Under the catalysis of thermally reduced iron nanoparticles (Fe NPs), nanometer-size graphene sheets were *in-situ* grown on the LFP surface through the realignment of carbon

fragments aroused from the pyrolysis of glucose. The graphene sheets not only form a compact and uniform coating layer along the LFP surface, but also stretch out and cross-link into a conducting network around the LFP particles. Therefore, the electrochemical performance of the mono-dispersed quasi-hexahedral LFP NPs obtained from a hydrothermal process is remarkably improved with the assistance of the graphene decorating. To the best of our knowledge, this is the first report about synthesizing graphene decorations for cathode materials using *in-situ* technique at low synthesis temperature. This low-cost and effective graphene surface decorating technique can be applied as a general strategy for more electroactive composite materials used in energy storage devices.

2. Experimental

2.1. Synthesis of LFP NPs and LFP@graphene composite

LFP NPs were synthesized through an optimized hydrothermal method. The starting materials of $\text{FeSO}_4 \cdot 7\text{H}_2\text{O}$ (AR grade), H_3PO_4 (85 wt%) and $\text{LiOH} \cdot \text{H}_2\text{O}$ (AR grade) were used as received. First, 0.25 mol $\text{LiOH} \cdot \text{H}_2\text{O}$ and 0.083 mol H_3PO_4 were dissolved into 150 mL de-ionized water under magnetic stirring. Then, 0.83 mol FeSO_4 aqueous solution was added to the $\text{LiOH}/\text{H}_3\text{PO}_4$ solution. The molar ratio of $\text{Li}:\text{Fe}:\text{P}$ was kept at 3:1:1. After stirring for 30 min under an argon gas, the resulting mixture was transferred into a 500-mL-capacity Teflon-lined stainless steel autoclave. The sealed autoclave was then placed into a 200 °C oven for 10 h. Subsequently, the autoclave was cooled down to room temperature and the resulting gray white precipitate (LFP powder) was filtered with de-ionized water and ethanol several times. Finally, the obtained powder was dried at 120 °C in vacuum for 2 h.

To prepare the LFP@graphene composite, D-(+)-glucose ($\text{C}_6\text{H}_{12}\text{O}_6 \cdot \text{H}_2\text{O}$, AR grade) and $\text{FeSO}_4 \cdot 7\text{H}_2\text{O}$ were chosen as the carbon source and the catalyst precursor, respectively. LFP NPs (1.58 g) were firstly mixed with $\text{FeSO}_4 \cdot 7\text{H}_2\text{O}$ and D-(+)-glucose, and the mole ratio between LFP and FeSO_4 varied from 50:1 to 500:1 while the mass ratio between LFP and carbon contained in glucose was kept at 95:5. After careful grinding, 100 mL Milli-Q (Millipore) water was put into the mixture. Under vigorous stirring, the mixture was heated at 100 °C till the water was completely evaporated. The dried mixture was put into a quartz boat and then transferred into the center of a tube furnace with the protection of Ar/H_2 (95:5) atmosphere. The furnace was heated up to 750 °C at the rate of 5 °C min^{-1} and held at this temperature for 6 h. After cooling down to room temperature, the as-prepared composites were used as the cathode material without further purification. As a reference, conventional LFP@amorphous carbon (LFP@AC) was synthesized under the same processing conditions in the absence of $\text{FeSO}_4 \cdot 7\text{H}_2\text{O}$ catalyst precursor.

2.2. Structural characterization

The percentage (wt%) of carbon (including amorphous carbon and graphene) in the as-prepared composites was estimated using a high-precision thermogravimetric analysis system (TG/DTA 7300, SII Nano Technology Inc., Shanghai) in a dry flowing air environment. Morphologies of the materials were observed with scanning electron microscopy (SEM) using a Hitachi S-4700 operated at 15 kV accelerating voltage. Transmission electron microscopy (TEM) micrographs and High-resolution transmission electron microscopy (HRTEM) micrographs were captured on the JEM-2100 instrument at an acceleration voltage of 200 kV. The elemental and structural analysis was identified by X-ray diffraction (XRD, PANalytical X'Pert PRO, Ni-filtered $\text{Cu K}\alpha$ radiation, Netherlands).

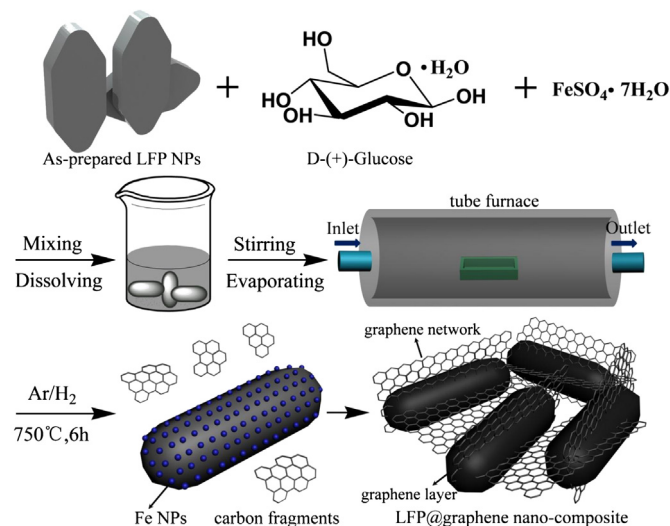


Fig. 1. A schematic drawing (not to scale) of the overall preparation of the LFP@graphene composite through an *in-situ* solid-state reaction.

Raman spectroscopy measurements (LabRam HR800, Jobin Yvon, France) were carried out using the excitation line of 514 nm from an argon-ion laser with 10 s exposure time, 70 mW power, 200 μm pinhole, 100 μm slit and 600 grating.

2.3. Electrochemical measurements

Working electrodes were prepared by casting slurries containing active materials (LFP@graphene or LFP@AC composites), polyvinylidene fluoride (PVDF) binder and conductive carbon black (SUPER P[®], TIMCAL Graphite & Carbon) onto a 20 μm -thick aluminum foil (99.99% purity). The slurry was prepared by mixing 84% active material, 8% PVDF and 8% conductive carbon black in NMP solvent. All the laminates were controlled to have an active material loading of *ca.* 3 mg cm^{-2} . The obtained electrodes were then dried at 120 $^\circ\text{C}$ in a vacuum oven for 12 h and pressed to enhance the adhesion between the electrode laminate and the Al substrate. Half cells were assembled in an Ar-filled glove box (<0.5 ppm of oxygen and water, OMNI-LAB, VAC) using commercial electrolyte consisting of 1 M LiPF_6 in ethylene carbonate/diethylene carbonate (EC/DEC, *v/v* = 1:1). Lithium metal foil (99.9% purity) was utilized as the counter electrode and a polypropylene film (Celgard 2400) was used as the separator. Galvanostatic charge–discharge cycling was performed on Maccor S4000 (Maccor Instruments,

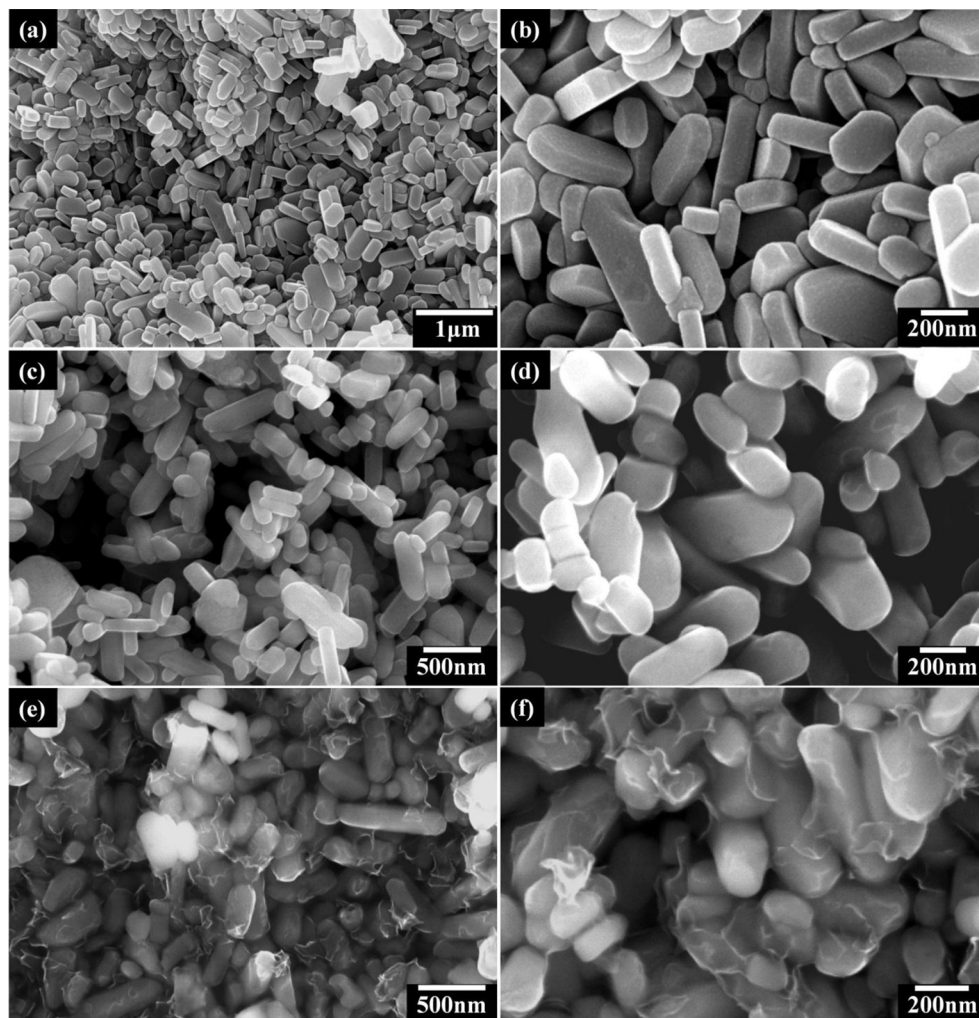


Fig. 2. SEM micrographs of (a)–(b) as-prepared LFP NPs, (c)–(d) LFP@AC composite, (e)–(f) LFP@graphene composite.

USA) between 2.0 V and 4.2 V. Charge and discharge rates were calculated according to the theoretical capacity of the LFP (170 mAh g⁻¹), all the electrodes were charged and discharged at the same rates until 5C, and then the charge rates were kept at 5C and the discharge rates varied from 10C to 100C. Cyclic voltammetry (CV) in the potential window of 2.5 V and 4.2 V at a rate of 0.1 mV s⁻¹ was performed on an Autolab potentiostat (PGSTAT302N, Autolab Instruments, Switzerland). Electrochemical impedance spectroscopy (EIS) was measured by applying an alternating voltage of 5 mV over the frequency ranging from 10⁻² to 10⁵ Hz. All impedance measurements were carried out at 40% DOD (depth of discharge) after the rate tests. Prior to the AC impedance measurements, the cell was rested for at least 3 h to attain the condition of sufficiently low residual current.

3. Results and discussion

As schematically shown in Fig. 1, the overall preparation of the LFP@graphene composite was accomplished through an *in-situ* solid-state process. As described in the experimental section, the dried mixture consisting of LFP NPs, glucose and FeSO₄ according to different mass (or mole) ratios was transferred into the center of the tube furnace, in which glucose and the trace amount of FeSO₄ were employed as the carbon source (including amorphous carbon and graphene) and catalyst precursors, respectively. Subsequently, the furnace was heated up to 750 °C and kept for 6 h. At this condition, glucose was completely pyrolyzed into carbon fragments and the trace of FeSO₄ can be thermally reduced to highly-ordered Fe NPs (shown in Fig. 1). Under the catalysis of Fe NPs, nanometer-size graphene sheets were *in-situ* grown on the LFP surface through the realignment of carbon fragments, and such graphene sheets not only form a compact and uniform coating layer throughout the LFP surface, but also stretch out and cross-link into a conducting network around the LFP particles. As a reference, LFP@AC composite was synthesized under the same processing conditions in the absence of FeSO₄ catalyst precursor.

Fig. 2 displays the SEM images of the as-prepared LFP NPs obtained from the hydrothermal process, LFP@AC and LFP@graphene composites at different magnifications. Clearly, the as-prepared LFP NPs (shown in Fig. 2a and b) were mono-dispersed nano-particles of irregular quasi-hexahedron plates with a length, width and thickness of 400–600 nm, 200–300 nm and 80–100 nm, respectively. It is generally accepted that the side length of 200–400 nm and thickness less than 100 nm are the optimal particle size for LFP material with high electrochemical performance [26,48]. Therefore, this would suggest, our hydrothermal sample is ideal in terms of dimensionality.

XRD pattern and Raman spectrum of the pristine LFP NPs are shown in Fig. 3a and b. As illustrated in Fig. 3a, the obtained pattern of LFP NPs shows well-crystallized diffraction peaks indexed to orthorhombic olivine LiFePO₄ (JCPDS No. 40-1499). No noticeable diffraction peaks associated with impurities (Fe₂O₃, Li₃PO₄, Fe₂P), typically reported in literature [49,50], are perceived in these samples, reflecting the high purity of the as-prepared LFP NPs. Raman spectrum of the LFP NPs shown in Fig. 3b confirms the structural information measured by XRD. Bands at 100–500 and 520–1120 cm⁻¹ correspond to the Raman vibrations of Fe–O and PO₄³⁻ in LiFePO₄, respectively [39,51–53].

Fig. 2c and d present the SEM micrographs of the LFP@AC composite. It is seen that the original shape and size of the LFP NPs are well maintained after annealing and carbon coating processes, except that the edges and corners become much sleeker. XRD pattern of the LFP@AC composite was presented in Fig. 3a, in which no typical diffraction peaks associated with carbonaceous materials are observed. This implies that the pyrolytic carbon is rather

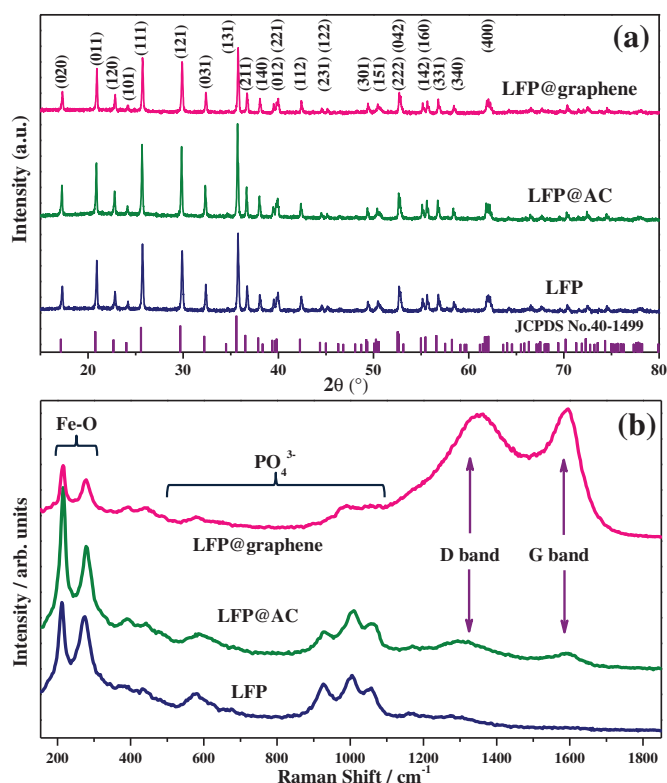


Fig. 3. (a) XRD patterns and (b) Raman spectra of the LFP NPs, LFP@AC and LFP@graphene composites.

amorphous or its typical peaks are eclipsed by the strong LFP peaks due to the small content of carbon involved. Raman spectrum of LFP@AC can provide more information about the carbon coating layer, as shown in Fig. 3b, disorder-induced D band and the graphitic G band are observed at ~1598 and ~1353 cm⁻¹, respectively [37,39,54,55]. The high I_D/I_G value of 1.18 indicates a low extent of graphitic carbon and a high concentration of defects. These results further confirm that the carbon coating layer in the LFP@AC composite is mainly amorphous carbon [26,27,37,39].

LFP@graphene composite was synthesized through *in-situ* pyrolysis and catalytic graphitization of glucose under the existence of highly dispersed Fe NPs. In order to explore the optimum catalyst content for graphene growth on the LFP surface, the mole ratios of LFP/FeSO₄ were chosen at 50:1, 100:1, 200:1 and 500:1. Fig. S1 (Supporting information) provides the SEM images of the as-prepared carbon-coated LFP at different LFP/FeSO₄ ratios. Clearly, the carbon morphology is strongly affected by the FeSO₄ additive content. As illustrated in Fig. S1, graphene network is only developed around the LFP NPs at a LFP/FeSO₄ molar ratio of 200:1. This is because the size and distribution of catalyst cluster are crucial to the carbon material growth (e.g. carbon nanotube and graphene) [56–60]. At low FeSO₄ concentration, the amount of the reduced Fe NPs is insufficient to catalyze the graphene growth (as shown in Fig. S1d). When the FeSO₄ additive content is too high, the size of the thermally reduced Fe NPs may be too large to catalyze the growth of graphene [56–60]. Therefore, a mole ratio of 200:1 between the LFP and FeSO₄ is the optimum catalyst content for *in-situ* growth of graphene.

SEM images of the representative LFP@graphene composite at different magnifications are shown in Fig. 2e and f. The nano-sized folding silk-like graphene sheets with fine transparent features are grown on the LFP surface. The micrographs suggest the graphene sheets cross-link into a conducting network connecting the LFP particles. As shown in Fig. 3a, just like the LFP@AC composite, no

typical diffraction peaks associated with carbonaceous materials are observed. However, Raman spectrum (Fig. 3b) shows an I_D/I_G value of 0.89, which is considerably lower than the 1.18 for LFP@AC composite synthesized in the absence of Fe catalyst [26,27,37,39]. The higher graphitization degree of the carbon coating layer for the LFP@graphene composite confirms that Fe NPs effectively promotes the growth of graphitic carbon during the pyrolysis and graphitization processes.

TEM images can provide more precise information about the structure, morphology and distribution of the carbon-decorated LFP composites. Fig. 4a and b shows the representative TEM and HRTEM images for the LFP@AC composite. As seen in Fig. 4a, each individual LFP@AC particle possesses a core/shell structure with an

integral but non-uniform amorphous carbon shell (red arrow (in the web version)). HRTEM image shown in Fig. 4b confirms that the carbon coating layer is amorphous as no typical graphitic layer is observed. It should be noted that the carbon layer is not quite uniform, and it is thin in some regions (*ca.* 4.9 nm) and thick in other places (*ca.* 10.9 nm), indicating random and irregular growth of the amorphous carbon layer.

Fig. 4c–e display the representative TEM and HRTEM images of the LFP@graphene composite. Loose and cross-linked graphene network is successfully formed and effectively surrounds and intrinsically connects the LFP particles. The regular in-plane lattice (inset in Fig. 4c) indicates that *in-situ* growing graphene sheets around LFP are highly graphitic. Fig. 4d presents the HRTEM image

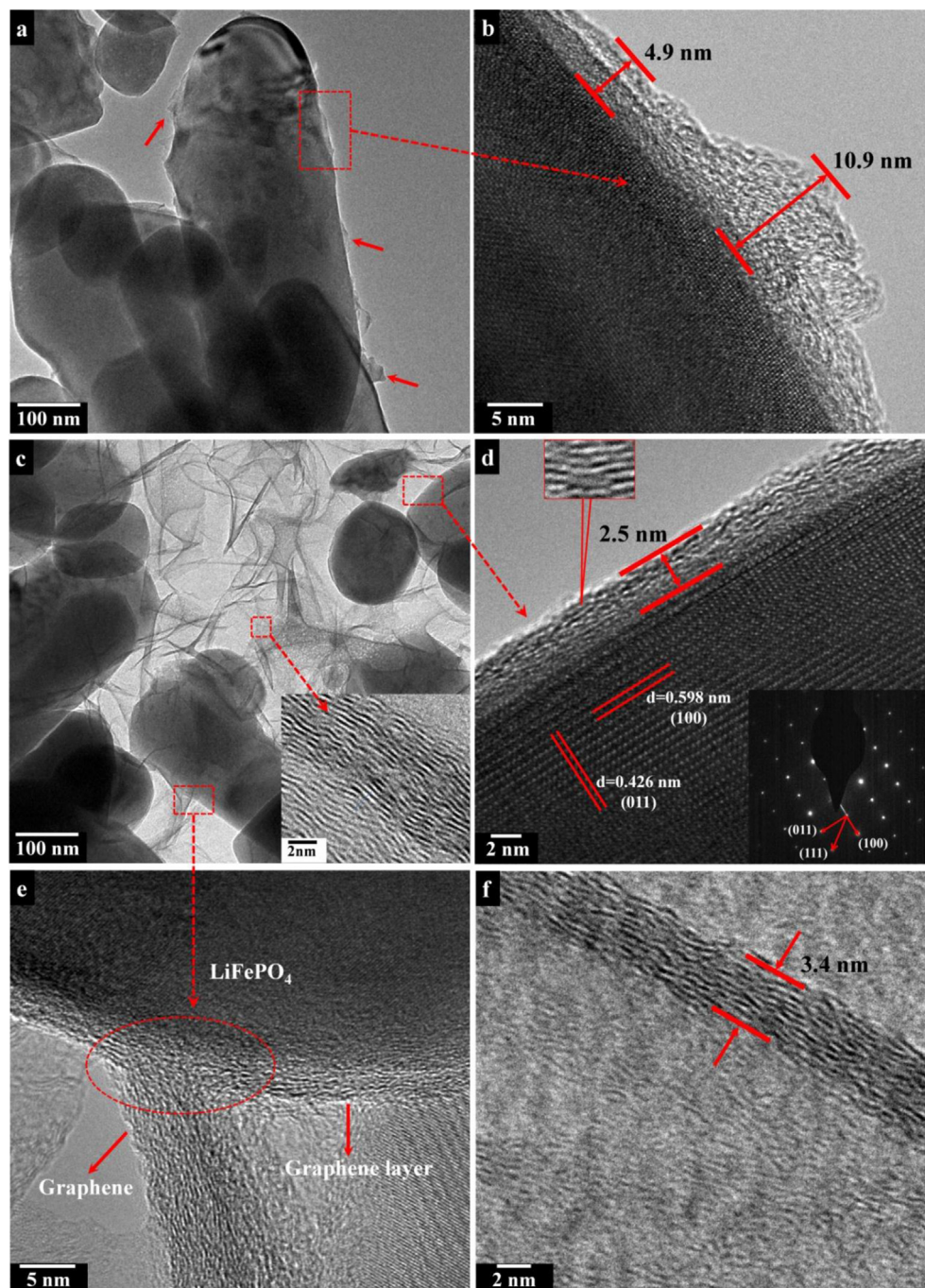


Fig. 4. TEM and HRTEM images of (a)–(b) LFP@AC composite, (c)–(e) LFP@graphene composite and (f) the edge of the *in-situ* growing graphene sheets.

of a typical LFP/graphene shell interface. It is clear that the graphene layer is grown along the LFP particle surface and is intrinsically combined with the LFP phase. The crystal lattice fringes of the LFP with the d-spacing of 0.598 and 0.426 nm are indexed to the (100) and (011) crystal planes of the orthorhombic LFP [40]. The graphene coating layer is very thin and uniform with an average thickness of *ca.* 2.5 nm (*i.e.* 8 layers). The crystal lattice fringes (shown in Fig. 4d and the inset) with an inter-planar spacing of *ca.* 0.34 nm corresponds to the d-spacing of (002) crystal plane (0.335 nm) of a typical graphite [54]. Fig. 4e provides the detailed information on the spreading of graphene sheet (red circle). Clearly, the graphene sheet is stretched out from the surface of the compact graphene shell, suggesting the pyrolytic carbon fragments tend to form the graphene “branches” after LFP particles are fully covered with a uniform graphene “skin”, thus constructing a conducting network. Fig. 4f displays the HRTEM image of the graphene sheet edge. It shows that the *in-situ* growing graphene sheets are composed of 8–9 layers, suggesting that the structure of the graphene sheets connecting the LFP NPs is consistent with that of the graphene shell throughout the LFP surface.

Carbon content of the LFP@AC and LFP@graphene composites was estimated by the thermogravimetric (TGA) technique and the results are shown in Fig. S2 (Supporting information). Theoretically, the oxidation of pure LFP phase to $\text{Li}_3\text{Fe}_2(\text{PO}_4)_3$ and Fe_2O_3 results in a weight gain of 5.07 wt% during annealing in air [40]. From the TGA curves, the total weight increment of the LFP@AC and LFP@graphene composites is 3.02 and 2.92 wt%, respectively. Carbon content of the LFP@AC and LFP@graphene composites is therefore calculated to be 2.05 (5.07 – 3.02) and 2.15 wt% (5.07 – 2.92), respectively. Neglecting the additional tiny weight change from oxidation of the trace Fe to Fe_2O_3 for the LFP@graphene composite, the carbon content of the two composites is comparable. Therefore, the effect of different carbon content on the electrochemical performance of LFP is ruled out.

Electrochemical behavior of the LFP@graphene composite was studied by comparison with the conventional LFP@AC material. CV plots of LFP@AC and LFP@graphene materials are shown in Fig. 5a. Both the two materials showed a pair of redox peaks at around 3.56 and 3.28 V, corresponding to the redox process between Fe^{3+} and Fe^{2+} [38–40]. By comparison, CV plot of the LFP@graphene material exhibited a more symmetrical and poignant shape of the anodic/cathodic peaks. The peak separation for the LFP@graphene electrode was *ca.* 0.225 V, which was approximately 68 mV smaller than the *ca.* 0.293 V for the LFP@AC electrode. It illustrates an easy kinetic process for Li ion insertion and extraction into and from the LFP@graphene material. In addition, the higher peak current of both the anodic and cathodic peaks for the LFP@graphene electrode indicates a higher electrochemical reactivity of the material.

Fig. 5b compares the first charge–discharge profiles of the LFP@AC and LFP@graphene materials at 0.1C ($1\text{C} = 170\text{ mAh g}^{-1}$). The typical flat potential plateau at 3.4 V (versus Li^+/Li) is associated with the Fe^{3+} and Fe^{2+} redox process [7,26,37,39,40,61]. The LFP@graphene electrode delivered a discharge capacity of *ca.* 167.7 mAh g^{-1} , which accounts for 98.65% of the theoretical capacity, revealing a high utility of the active materials. By contrast, the discharge capacity for the LFP@AC electrode is only 153 mAh g^{-1} (*ca.* 90% of the theoretical capacity). Furthermore, the polarization evaluated from the difference between the charge and discharge plateaus was 49.6 and 98.6 mV for the LFP@graphene and LFP@AC electrodes, respectively, indicating an easy kinetic process for the LFP@graphene composite. The superior Li storage performance can be attributed to the high electronic conductivity and ionic diffusivity of the LFP@graphene composite due to the full coverage and intrinsic connection between the graphene layer and LFP NPs. Also, the highly conducting graphene network contributes a lot to the total electronic conductivity, especially the electron transfer between LFP NPs.

High power of LFP electrode without an undue sacrifice in energy density is always an important goal for the material synthesis and optimizations. Rate performance of the LFP@AC and LFP@graphene electrodes was investigated and the results are provided in Fig. 6a (Rate performance of the carbon-coated or graphene-decorated LFP samples prepared at different LFP/ FeSO_4 ratios from 50 to 500 is presented and discussed in Fig. S3 in the Supporting information). It should be noted that the electrodes were charged and discharged at the same rates until 5C, and then the charge rates were kept at 5C and the discharge rates varied from 10C to 100C. Obviously, the LFP@graphene electrode exhibited a much improved rate capability. It was able to deliver a discharge capacity of 152.2 mAh g^{-1} at 10C, 118.1 mAh g^{-1} at 50C and 94.3 mAh g^{-1} at 100C. By contrast, the LFP@AC electrode exhibited 137.6, 112.7, and 61.4 mAh g^{-1} at 10, 50 and 100C, respectively. Discharge curves of the LFP@AC and LFP@graphene electrodes at different rates are shown in Fig. 6b. With the increase of discharge rates, the lowering trend of discharge curves is due to the polarization induced by the internal resistance of the electrode. It is clear that the onset discharge plateau for the LFP@AC electrode at 50, 80 and 100C was lowered to 2.80, 2.51, and 2.27 V, respectively, very close to the cut-off voltage of 2.0 V. By contrast, the onset discharge plateau for the LFP@graphene electrode at 50, 80 and 100C was maintained at 3.15, 3.02 and 2.92 V, respectively. The comparison shows that the higher capacity loss of the LFP@AC electrode at high rate is mainly coming from the high internal resistance of the electrode and the resistance is considerably reduced by *in-situ* growing graphene decorations for the LFP@graphene electrode [62].

To further explain the electrochemical behavior of the LFP@AC and LFP@graphene electrodes, the electrochemical kinetic

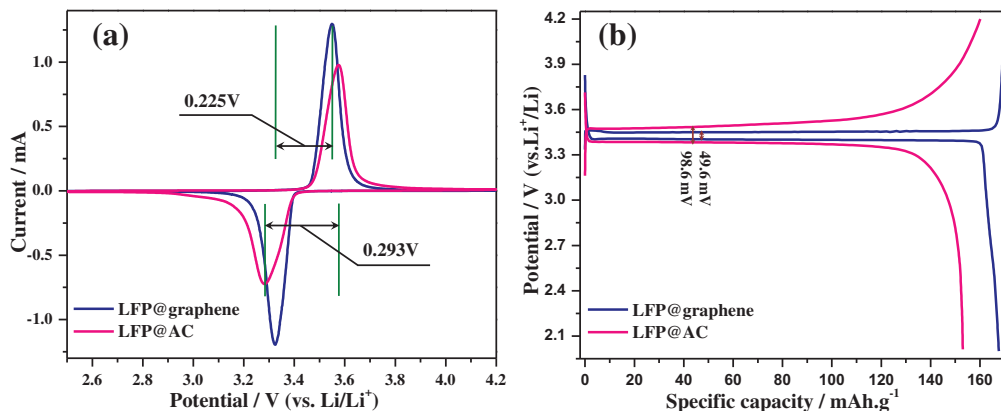


Fig. 5. (a) CV curves and (b) first galvanostatic charge–discharge profiles of the LFP@AC and LFP@graphene electrodes.

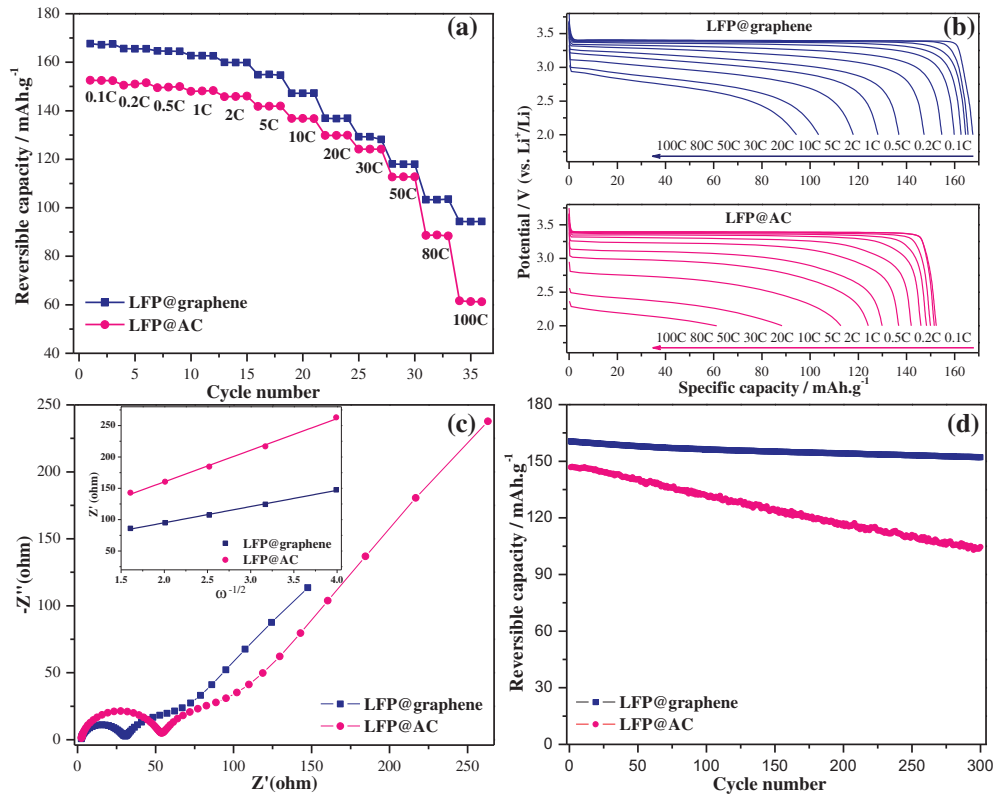


Fig. 6. (a) Rate performance of the LFP@AC and LFP@graphene electrodes, (b) discharge curves of the LFP@AC and LFP@graphene electrodes at various C rates, (c) Nyquist plots of the LFP@AC and LFP@graphene electrodes at 40% DOD and plots of Z' versus the square root of frequency (the inset), (d) plots of reversible discharge capacity versus cycle number for the LFP@AC and LFP@graphene electrodes.

performance of the two cathodes was analyzed with the EIS measurements. Fig. 6c shows the Nyquist plots of the LFP@AC and LFP@graphene electrodes measured at 40% DOD. Each spectrum consists of two semi-circles and a slope. Previous studies have associated the high-to-mid-frequency semicircle with the surface film or solid electrolyte interphase (SEI) film formed on the cathode [63,64]. According to our understanding, it is more likely to be related to the particle-to-particle interfacial contact resistance given the semicircle is greatly affected by the physical properties including chemical composition, electronic conductivity and electrode porosity [65,66]. The semicircle in the mid-to-low-frequency range, referred to be a measure of the charge-transfer resistance at the electrolyte/electrode interface [67,68]. The slope line at the lowest frequencies is attributed to the diffusion of lithium ions within the electrode [65–68]. As seen in Fig. 6c, a very small high-to-mid-frequency semicircle for the LFP@graphene electrode implies the low contact resistance (31.2 Ω) between active material particles. As for the LFP@AC electrode, the contact resistance is calculated to be 53.5 Ω. These results are in good agreement with the difference in the rate performance of the two electrodes exhibited in Fig. 6a.

To examine the diffusion kinetics of lithium ions in the LFP@AC and LFP@graphene composites, we further calculate the Li ion diffusion coefficient (D) from the slope line at the lowest frequency according to the following relation [30]:

$$D = (R^2 T^2) / (2 A^2 n^4 F^4 C^2 \sigma^2) \quad (1)$$

where n is electron number for each molecule during Li⁺ ion insertion, A is the surface area of the cathode, F is the Faraday constant, C is Li⁺ ion concentration, and σ is the Warburg factor. σ is related with Z' as:

$$Z' \propto \sigma \omega^{-1/2} \quad (2)$$

In which Z' represents the real part of the resistance in the low-frequency region and ω is the corresponding frequency. The relationship between Z' and the square root of frequency in the low-frequency region is shown in the inset plot of Fig. 6c. From this plot, Li⁺ ion diffusion coefficients (D) are calculated to be 1.5×10^{-14} and 6.0×10^{-14} cm² s⁻¹ for the LFP@AC and LFP@graphene electrodes, respectively, indicating that Li ion diffusion in the LFP@graphene composite is much faster than in the LFP@AC composite. This further confirms that the *in-situ* growing ultra-thin graphene coating layer and the cellular graphene network is helpful to the rapid Li ion transport.

Fig. 6d provides the cycling performance of the LFP@AC and LFP@graphene electrodes at 1C charge and 1C discharge rates. After 300 charge–discharge cycles, the LFP@AC electrode retained a discharge capacity of 104.5 mAh g⁻¹, corresponding to the capacity retention of 71.2%. Meanwhile, the LFP@graphene electrode retained discharge capacities of 152.2 and 145.5 mAh g⁻¹ after 300 and 550 cycles (Fig. S4 in the Supporting information), corresponding to capacity retentions of 94.8% and 90.7%, respectively. In addition, cycling performance of the LFP@graphene electrode at 20C charge and 20C discharge rates is also provided in Fig. S5 (Supporting information), which retains a discharge capacity of 78.8 mAh g⁻¹ after 200 cycles corresponding to capacity retention of 87.1%, suggesting a stable cycling capability at high charge/discharge rates.

It should be noted that most of nano-LFP material prepared through wet methods shows poor cycling performance due to the interaction between the nano-particles and the electrolyte. The cycling stability improvement by *in-situ* growing graphene coatings

can be attributed to the very uniform graphitic carbon coating layer which effectively suppress the interaction between the LFP and the electrolyte. By the way, it's worth mentioning that the trace of Fe NPs didn't show any negative effect on the electrochemical behavior of the LFP/graphene electrode. This may be because that the very small amount of Fe particles is entirely encapsulated during the graphene growth and is separated from the electrolyte.

4. Conclusion

In this work, a graphene-decorated LFP composite was synthesized through *in-situ* pyrolysis and catalytic graphitization. At a molar ratio of LFP/FeSO₄ 200:1, the reduced Fe NPs can catalyze the growth of graphene sheets on the LFP surface through the realignment of carbon fragments aroused from pyrolysis of glucose under Ar/H₂ (95:5) at 750 °C. The *in-situ* growing graphene sheet contains 8–9 layers and has an average thickness of about 2.5 nm. It can not only form a compact and uniform coating layer along the LFP surface, but also stretch out and cross-link into a conducting network around the LFP particles. This graphene-decorating structure contributes to a remarkable improvement of the electrical conductivity and the unenclosed cellular graphene network allows the rapid Li ion transport. The LFP/graphene composite attained a high reversible capacity of 167.7 mAh g⁻¹ at 0.1C, superb rate performance and prolonged cycle life. This low-cost and effective surface decorating strategy may provide a broadly applicable route for more electroactive materials used in energy storage devices.

Acknowledgments

The authors are greatly indebted to the funding of Natural Science Foundation of China (NSFC, contract no. 51272168, 21203132 and 21203134).

Appendix A. Supplementary data

Supplementary data related to this article can be found at <http://dx.doi.org/10.1016/j.jpowsour.2013.10.106>.

References

- [1] A.K. Padhi, K.S. Nanjundaswamy, J.B. Goodenough, *J. Electrochem. Soc.* 144 (1997) 1188–1194.
- [2] A. Yamada, S.C. Chung, K. Hinokuma, *J. Electrochem. Soc.* 148 (2001) A224–A229.
- [3] M.S. Whittingham, *Chem. Rev.* 104 (2004) 4271–4301.
- [4] K.S. Park, S.B. Schougaard, J.B. Goodenough, *Adv. Mater.* 19 (2007) 848–851.
- [5] L. Kavan, I. Exnar, J. Cech, M. Graetzel, *Chem. Mater.* 19 (2007) 4716–4721.
- [6] H.H. Zheng, L.L. Chai, X.Y. Song, V.S. Battaglia, *Electrochim. Acta* 63 (2012) 256–262.
- [7] L. Wang, X.M. He, W.T. Sun, J.L. Wang, Y.D. Li, S.S. Fan, *Nano Lett.* 12 (2012) 5632–5636.
- [8] L.X. Yuan, Z.H. Wang, W.X. Zhang, X.L. Hu, J.T. Chen, Y.H. Huang, J.B. Goodenough, *Energy Environ. Sci.* 4 (2011) 269–284.
- [9] Y.G. Wang, P. He, H.S. Zhou, *Energy Environ. Sci.* 4 (2011) 805–817.
- [10] R. Amin, P. Balaya, J. Maier, *Electrochem. Solid-State Lett.* 10 (2007) A13–A16.
- [11] Y.G. Wang, Y.R. Wang, E.J. Hosono, K.X. Wang, H.S. Zhou, *Angew. Chem. Int. Ed.* 47 (2008) 7461–7465.
- [12] D. Morgan, A. Van der Ven, G. Ceder, *Electrochem. Solid-State Lett.* 7 (2004) A30–A32.
- [13] B.L. Ellis, W.R.M. Makahnouk, Y. Makimura, K. Toghill, L.F. Nazar, *Nat. Mater.* 6 (2007) 749–753.
- [14] C. Delacourt, P. Poizat, S. Levasseur, C. Masquelier, *Electrochem. Solid-State Lett.* 9 (2006) A352–A355.
- [15] C. Delmas, M. Maccario, L. Croguennec, F. Le Cras, F. Weill, *Nat. Mater.* 7 (2008) 665–671.
- [16] J. Liu, T.E. Conry, X.Y. Song, M.M. Doeff, T.J. Richardson, *Energy Environ. Sci.* 4 (2011) 885–888.
- [17] C.W. Sun, S. Rajasekhara, J.B. Goodenough, F. Zhou, *J. Am. Chem. Soc.* 133 (2011) 2132–2135.
- [18] Y.S. Hu, Y.G. Guo, R. Dominko, M. Gaberscek, J. Jamnik, J. Maier, *Adv. Mater.* 19 (2007) 1963–1966.
- [19] F. Croce, A. D'Epifanio, J. Hassoun, A. Deptula, T. Olczac, B. Scrosati, *Electrochem. Solid-State Lett.* 5 (2002) A47–A50.
- [20] R. Dominko, J.M. Goupil, M. Bele, M. Gaberscek, M. Remskar, D. Hanzel, J. Jamnik, *J. Electrochem. Soc.* 152 (2005) A858–A863.
- [21] R. Dominko, M. Bele, M. Gaberscek, M. Remskar, D. Hanzel, S. Pejovnik, J. Jamnik, *J. Electrochem. Soc.* 152 (2005) A607–A610.
- [22] G.L. Cui, L. Gu, L.J. Zhi, N. Kaskhedikar, P.A. van Aken, K. Mullen, J. Maier, *Adv. Mater.* 20 (2008) 3079–3083.
- [23] S.Y. Chung, J.T. Bloking, Y.M. Chiang, *Nat. Mater.* 1 (2002) 123–128.
- [24] S.B. Schougaard, J. Breger, M. Jiang, C.P. Grey, J.B. Goodenough, *Adv. Mater.* 18 (2006) 905–909.
- [25] M.S. Song, D.Y. Kim, Y.M. Kang, Y.I. Kim, J.Y. Lee, H.S. Kwon, *J. Power Sources* 180 (2008) 546–552.
- [26] J.J. Wang, X.L. Sun, *Energy Environ. Sci.* 5 (2012) 5163–5185.
- [27] H.Q. Li, H.S. Zhou, *Chem. Commun.* 48 (2012) 1201–1217.
- [28] K. Saravanan, P. Balaya, M.V. Reddy, B.V.R. Chowdari, J.J. Vittal, *Energy Environ. Sci.* 3 (2010) 457–464.
- [29] M. Gaberscek, R. Dominko, J. Jamnik, *Electrochem. Commun.* 9 (2007) 2778–2783.
- [30] Y.K. Zhou, J. Wang, Y.Y. Hu, R. O'Hayre, Z.P. Shao, *Chem. Commun.* 46 (2010) 7151–7153.
- [31] Z.D. Huang, S.W. Oh, Y.B. He, B. Zhang, Y. Yang, Y.W. Mai, *J. Mater. Chem.* 22 (2012) 19643–19645.
- [32] Y.Q. Hu, M.M. Doeff, R. Kostecki, R. Finones, *J. Electrochem. Soc.* 151 (2004) A1279–A1285.
- [33] J.K. Kim, G. Cheruvally, X. Li, J.H. Ahn, K.W. Kim, H.J. Ahn, *J. Phys. Chem. Solids* 69 (2008) 1257–1260.
- [34] M.M. Doeff, Y.Q. Hu, F. McLarnon, R. Kostecki, *Solid-State Lett.* 6 (2003) A207–A209.
- [35] N. Ravet, M. Gauthier, K. Zaghib, J.B. Goodenough, A. Mauger, F. Gendron, C.M. Julien, *Chem. Mater.* 19 (2007) 2595–2602.
- [36] A.A. Salah, A. Mauger, K. Zaghib, J.B. Goodenough, N. Ravet, M. Gauthier, F. Gendron, C.M. Julien, *J. Electrochem. Soc.* 152 (2006) A1692–A1701.
- [37] X.F. Zhou, F. Wang, Y.M. Zhu, Z.P. Liu, *J. Mater. Chem.* 21 (2011) 3353–3358.
- [38] B. Wang, D.L. Wang, Q.M. Wang, T.F. Liu, C.F. Guo, X.S. Zhao, *J. Mater. Chem. A* 1 (2013) 135–144.
- [39] Y. Shi, S.L. Chou, J.Z. Wang, D. Wexler, H.J. Li, H.K. Liu, Y.P. Wu, *J. Mater. Chem.* 22 (2012) 16465–16470.
- [40] J.L. Yang, J.J. Wang, Y.J. Tang, D.N. Wang, X.F. Li, Y.H. Hu, R.Y. Li, G.X. Liang, T.K. Sham, X.L. Sun, *Energy Environ. Sci.* 6 (2013) 1521–1528.
- [41] H. Bi, F.Q. Huang, Y.F. Tang, Z.Q. Liu, T.Q. Lin, J. Chen, W. Zhao, *Electrochim. Acta* 88 (2013) 414–420.
- [42] Y. Ding, Y. Jiang, F. Xu, J. Yin, H. Ren, Q. Zhuo, Z. Long, P. Zhang, *Electrochem. Commun.* 12 (2010) 10–13.
- [43] L.H. Hu, F.Y. Wu, C.T. Lin, A.N. Khlobystov, L.J. Li, *Nat. Commun.* 4 (2013) 1687–1687-7.
- [44] Z.S. Feng, C. Zhang, J.J. Chen, Y. Wang, X. Jin, R. Zhang, J. Hu, *RSC Adv.* 3 (2013) 4408–4415.
- [45] Y. Zhang, W.C. Wang, P.H. Li, Y.B. Fu, X.H. Ma, *J. Power Sources* 210 (2012) 47–53.
- [46] Y.F. Tang, F.Q. Huang, H. Bi, Z.Q. Liu, D.Y. Wan, *J. Power Sources* 203 (2012) 130–134.
- [47] F.Y. Su, C.H. You, Y.B. He, W. Lv, W. Cui, F.M. Jin, B.H. Li, Q.H. Yang, F.Y. Kang, *J. Mater. Chem.* 20 (2010) 9644–9650.
- [48] W.J. Zhang, *J. Power Sources* 196 (2011) 2692–2970.
- [49] K. Dokko, K. Shirashi, K. Kanamuraa, *J. Electrochem. Soc.* 152 (2005) A2199–A2202.
- [50] C.L. Hu, H.H. Yi, H.S. Fang, B. Yang, Y.C. Yao, W.H. Ma, Y.N. Dai, *Mater. Lett.* 65 (2011) 1323–1326.
- [51] E. Markevich, R. Sharabi, O. Haik, V. Borgel, G. Salitra, D. Aurbach, G. Semrau, M.A. Schmidt, N. Schall, C. Stinner, *J. Power Sources* 196 (2011) 6433–6439.
- [52] Y. Bai, Y.F. Yin, J.M. Yang, C.B. Qing, W.F. Zhang, *J. Raman Spectrosc.* 42 (2011) 831–838.
- [53] C.M. Burba, J.M. Palmer, B.S. Holinsworth, *J. Raman Spectrosc.* 40 (2009) 225–228.
- [54] Z.W. Xu, H.J. Li, W. Li, G.X. Cao, Q.L. Zhang, K.Z. Li, Q.G. Fu, J. Wang, *Chem. Commun.* 47 (2011) 1166–1168.
- [55] K. Evanoff, A. Magasinski, J.B. Yang, G. Yushin, *Adv. Energy Mater.* 1 (2011) 495–498.
- [56] M. Corrias, B. Caussat, A. Ayral, J. Durand, Y. Kihn, P. Kalck, P. Serp, *Chem. Eng. Sci.* 58 (2003) 4475–4482.
- [57] K. Hata, D.N. Futaba, K. Mizuno, T. Namai, M. Yumura, S. Iijima, *Science* 306 (2004) 1362–1364.
- [58] L. Zhang, C.M.B. Holt, E.J. Luber, B.C. Olsen, H.T. Wang, M. Danaie, X.W. Cui, X.H. Tan, V.W. Liu, W.P. Kalisvaart, D. Mitlin, *J. Phys. Chem. C* 115 (2011) 24381–24393.
- [59] L. Zhang, L.Y. Wang, C.M.B. Holt, B. Zahir, Z. Li, K. Malek, T. Navessin, M.H. Eikerling, D. Mitlin, *Energy Environ. Sci.* 5 (2012) 6156–6172.
- [60] G.D. Nessim, D. Acquaviva, M. Seita, K.P. O'Brien, C.V. Thompson, *Adv. Funct. Mater.* 20 (2010) 1306–1312.
- [61] L. Laffont, C. Delacourt, P. Gibot, M.Y. Wu, P. Kooyman, C. Masquelier, J.M. Tarascon, *Chem. Mater.* 18 (2006) 5520–5529.
- [62] S.W. Oh, H.J. Bang, S.T. Myung, Y.C. Bae, S.M. Lee, Y.K. Sun, *J. Electrochem. Soc.* 155 (2008) A414–A420.

- [63] D. Aurbach, M.D. Levi, E. Levi, H. Teller, B. Markovsky, G. Salitra, U. Heider, L. Heider, *J. Electrochem. Soc.* 145 (1998) 3024–3034.
- [64] Y.G. Ryu, S.I. Pyun, *J. Electroanal. Chem.* 433 (1997) 97–105.
- [65] G. Liu, H. Zheng, S. Kim, Y. Deng, A.M. Minor, X. Song, V.S. Battaglia, *J. Electroanal. Chem.* 155 (2008) A887–A892.
- [66] H.H. Zheng, K. Jiang, T. Abe, Z. Ogumi, *Carbon* 44 (2006) 203–210.
- [67] C.S. Wang, A.J. Appleby, F.E. Little, *J. Electroanal. Chem.* 497 (2001) 33–46.
- [68] A. Funabiki, M. Inaba, Z. Ogumi, S. Yuasa, J. Otsuji, A. Tasaka, *J. Electrochem. Soc.* 145 (1998) 172–178.